Journal of the European Ceramic Society **17** (1997) 1201–1212

PII: S0955-2219(96)00213-0
0955-2219/97/$17.00 + 0.00

Dimensional Variation of Die-Pressed Ceramic Green Compacts: Comparison of a Finite Element Modelling with Experiment

I. Aydin,[a] B. J. Briscoe[a]* and K. Y. Sanliturk[b]

[a]Department of Chemical Engineering and Chemical Technology, Imperial College of Science, Technology and Medicine, London SW7 2BY, UK
[b]Department of Mechanical Engineering, Imperial College of Science, Technology and Medicine, London SW7 2BY, UK

(Received 30 May 1996; revised version received 11 October 1996; accepted 21 October 1996)

Abstract

The dimensional variation of simple die-pressed ceramic green compacts is analysed by elasto-plastic numerical modelling with the finite element method and also by experimental investigations. For the experimental investigations, the shape of a cylindrical alumina compact, obtained by using a single-acting punch die pressing system, was measured by means of non-contacting laser profilometry. To facilitate the numerical modelling, the Drucker–Prager/cap elasto-plasticity model was used in conjunction with the finite element code ABAQUS. Computed internal stress distributions are reported at various stages of the compaction. Also, the final geometry of the compacted green component was predicted. The origins of the dimensional variation of the ceramic green compacts are discussed. It is shown that the predicted shape results, obtained from the numerical model, agree well with the corresponding experimental results. © *1997 Elsevier Science Limited.*

1 Introduction

A common and rudimentary requirement of ceramic products is the production of components of prescribed overall dimensions within specified tolerances.[1] These parts are frequently produced by the sintering of compacted powders or 'green bodies' fabricated within die cavities. For instance, in the production of uranium dioxide nuclear fuel pellets, the accuracy of the cylindrical pellet dimensions and the absence of excessive depressions at the surfaces or corners are essential if the optimum performance is to be achieved. It is also extremely desirable that the fuel element cans have their final profile in closely controlled dimensional ranges.[2] Post-manufacture machining by grinding is not only expensive but also introduces defects. Similarly, in the fabrication of ceramic ball bearings or taper bearings the requisite degree of roundness or taper of the bearing is often difficult to achieve if the fabrication process for the ceramic involves unidirectional pressing. The subsequent grinding and polishing of the ball, after sintering, results in non-uniformity.[3] Hence, a means to predict the external shape of these types of ceramic green precursors is a common request of many manufacturing operations. The present paper examines a route for such a prediction and compares the predicted results with experiment.

Asymmetric die-pressing, the technique used in the present study, is the commonest consolidation technique, amongst several available, for the mass production of ceramic components.[4] In a die-pressing process, a controlled quantity of granulate is introduced into the die cavity. The cavity is closed using the plunger or upper part of the die, and the green forming pressure is then applied. At the final stage of the compaction cycle, the applied pressure is removed and the sample is ejected from the confines of the die wall. As a result of these various operations a green body is obtained which contains a degree of structural inhomogeneity of two kinds, namely, density distributions as the variation of the internal form and the dimensional variability as manifest in the external shape of the compact. The latter is the geometry of the external surface of the ceramic green body which is invariably not exactly the same as, or indeed a simple

*To whom correspondence should be addressed

linear scale transformation of, the shape of the terminal geometry of die cavity after the green ejection. There has been significant progress in understanding the nature of the internal form of die-pressed ceramic compacts.[5–8] However, important questions remain regarding the evolution of the external shape and the formation of the final geometry of the green compacts during the compaction process. The purpose of the present paper is to describe, by means of experiment, the dimensional variability of geometrically simple ceramic green compacts and also to provide a theoretical model to predict the same. The density distribution component of the current study is addressed elsewhere.[9] A numerical modelling from which the effect of internal structural inhomogeneity can be related to the external shape evolution during the compaction cycle also improves the understanding of the 'lamination' or 'capping' phenomenon which is frequently encountered especially in the pharmaceutical tabletting industry.

In the present paper, the shape of an alumina green compact, measured experimentally, and the evolution of shape of the compact, predicted by numerical modelling, during compaction are studied. The final shape of the cylindrical compact is measured by means of non-contacting laser profilometry. An elasto-plasticity model, known as the Drucker–Prager/cap model, is implemented for the analysis of the structural inhomogeneity and dimensional variability of the ceramic compacts by using the finite element code ABAQUS (Hibbitt, Karlsson and Sorensen, Inc., USA, version 5.4). The aim of the simulation component of study is to obtain quantitative information regarding the internal structural inhomogeneity and the external dimensional variability of the ceramic precursors. Stress distributions and shape evolution are obtained at each stage of the compaction process. A comparison of the experimental and the numerically predicted shape data is given in the later part of the paper. It is anticipated that this information may be used in the mathematical modelling of the mechanisms of the shape change which occurs in ceramic wares during their densification as a function of the processing parameters such as the forming stress, the tool–material interface condition and aspect (height to diameter) ratio of the compact.

2 Experimental Procedure

The following experimental study was implemented to provide a validation for the numerical results presented subsequently in this paper. The experimental procedure comprised the preparation of ceramic cylindrical compacts by means of uniaxial compaction and the measurement of overall shape of the unconstrained green bodies by means of non-contacting laser profilometry.

2.1 Preparation of the cylindrical ceramic green form

An α-Al_2O_3 powder (AKP-30, Sumitomo Chemicals Co. Ltd, Japan) of high purity (more than 99·99%, mean particle size 0·4 μm) was agglomerated by a pan granulation method[10] to achieve the necessary flow response for satisfactory die filling and pressing. The binder, 1% (w/w) in 10% aqueous solution, was a commercial poly(vinyl alcohol) (PVA), of *ca.* 72 000 molecular weight (BDH Chemicals Ltd, UK). The experiments to be discussed were conducted with the irregular-shaped alumina agglomerates in the range of 53–106 μm obtained by conventional sieving methods.[11]

The compaction was achieved by using a cylindrical steel die (internal diameter, D_i; 12·980 mm) mounted in a standard universal testing machine (Model 6022, Instron, UK). The arrangement is shown in Fig. 1. The pressing forces applied at the top punch and the displacement of the top punch, during the compaction, were recorded continuously as a function of time using a load sensor (LS in Fig. 1), available in the machine, and a separate linear variable displacement transducer (LVDT in Fig. 1(b)) (MD2·5, Schlumberger Industries, UK), respectively, by a data acquisition system (TP and HC in Fig. 1(a)). The control system for the testing machine (CS in Fig. 1(a)) enabled the compaction experiments to be undertaken in either displacement limited or load limited modes.

The compaction experimental procedure was as follows. A 'preform' was prepared in order to measure the compact characteristics accurately before starting the main compacting process. The die, supported upon the base together with its lower cylindrical punch, was filled with a fixed quantity of the alumina powder. The upper punch was then inserted into the die and the powder was compressed to a low pressure, *ca.* 3 MPa. The preform was then ejected and examined by measurements of its weight (RC210D, Sartorious AG, Germany) with a resolution of less than 0·02 mg and height between top and bottom surfaces (Digimatic Micrometer, Mitutoyo Ltd, Japan) with a resolution of 1 μm. These types of data are subsequently classified as 'before compaction' (see Table 1).

The preform was then reinserted into the die using the lower and upper punches as guides. The upper punch was lowered with the preform and entered into the die such that there was no separation between upper punch–preform–lower

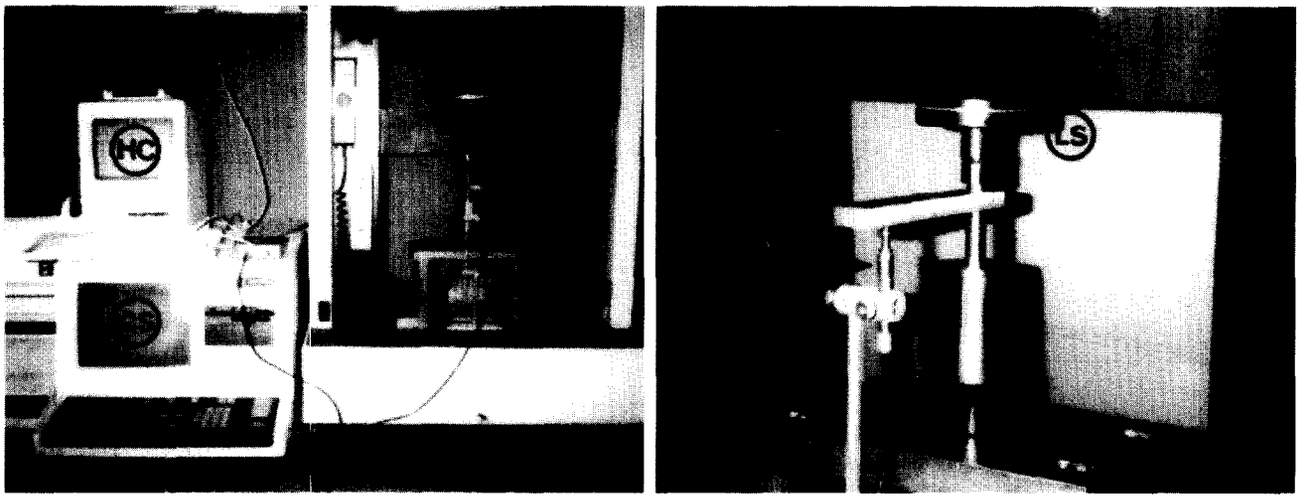

(a) (b)

Fig.1. Equipment used for pressing and monitoring the compaction process variables.

punch interfaces. The die walls were lubricated with zinc stearate powder (FSA Laboratory Supplies, UK). After insertion, the ram of the universal testing machine was moved downwards in small steps so as to achieve the initial contact between the force sensor and the upper punch of the die. The loading direction was reversed rapidly, without any significant dwell time, when the maximum applied force value, set by the control software, was reached. The applied maximum compacting stress, $\bar{\sigma}_{max}$, was 59·5 MPa. After the complete unloading the sample was ejected by first removing the lower punch and then using the upper punch to drive the sample out of the cylindrical die. The green body was then characterised geometrically as described in the next section. The height value of the compact after unloading was corrected, according to the recorded data, to counteract the influence of the instrument deflection. A typical plot of the compact height, Z, versus the mean applied compressive stress, $\bar{\sigma}$, obtained from the compaction experiment during the loading and unloading phases, is depicted in Fig. 2. A summary of the compacting conditions adopted in the present study is given in Table 1.

2.2 Measurement of the external overall shape of the green compacts

A non-contacting laser scanning profilometer, with associated hardware and software, was used for the determination of the overall shape of the cylindrical green alumina compacts. In this paper, only the diametrical deviations of the cylindrical component are considered. It was assumed that the green samples were axisymmetric with a linear cylindrical axis. The measuring system is shown in Fig. 3. The laser sensor (LP in Fig. 3, LM200, Matsushita Automation Controls, Japan) which was used for the diametric measurements had a working distance of 30 ± 3 mm with a resolution of 1 μm. The output of the sensor signal was monitored by a host computer (HC in Fig. 3(a)) via a terminal panel (TP in Fig. 3(a)). The sample was supported by a special fixture which in turn was mounted on a tilting stage (TS in Fig. 3(b)) (Miniature Kinematic Tilting Stage, Ealing Optics, UK) which facilitated X and Y tilt adjustments (see Fig. 3(b)). The tilting stage was mounted on a manual X-positioner (MP in Fig. 3(b)) (Standard Range, Ealing Optics, UK). The arrangement enabled movement in the Y-direction by a precision translation stage (PTS in

Table 1. Experimental conditions

Modulus of compaction	Single action
Geometry of the die	Cylinder
Internal diameter of the die, D_i	12·980 mm
Compact weight, W	5·015 g
Applied maximum compacting stress, $\bar{\sigma}_{max}$	59·5 MPa
Velocity of compacting (loading and unloading)	5 mm min^{-1}
Density of the compact before compaction, ρ_0	1·737 g cm^{-3} (43·6% TD)[a]
Height of the compact before compaction, Z_0	21·820 mm
Density of the compact at maximum applied stress, $\rho_{\bar{\sigma}_{max}}$	2·155 g cm^{-3} (54·1% TD)
Height of the compact at maximum applied stress, $Z_{\bar{\rho}_{max}}$	17·280 mm
Height of the compact after unloading (corrected), $(Z_{UL})_{exp}$	17·590 mm

[a]Theoretical density (TD), 3·986 g/cm^3 for alumina powder

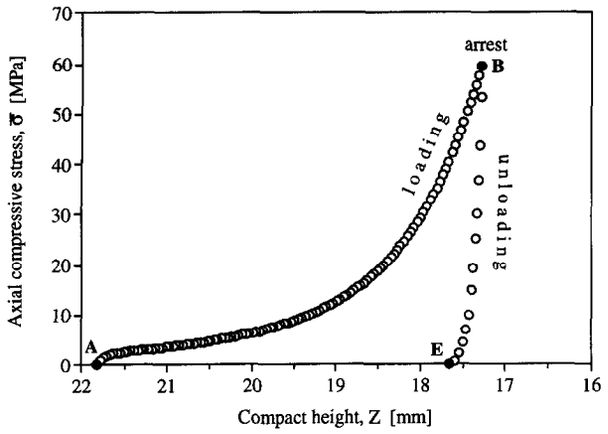

Fig. 2. Axial stress–compact height relation during loading and unloading phases in uniaxial compaction of the alumina sample (see Table 1 for the height values of the compact before compaction, at point A, at maximum applied stress, at point B, and after unloading, at point E).

Fig. 3) (PTS1000M, Photon Control, UK) controlled by a complete control system. The motion control system for the translation stage consisted of a driver unit (DU in Fig. 3(a)) (D3, Photon Control, UK) and a multifunction interface card (MIC, Photon Control, UK) fitted in a personal computer (PC in Fig. 3(a)) driven by the associated software.

The procedure for the overall shape measurement of the cylindrical ceramic green components which was implemented without delay after the compaction was as follows. The sample was moved between its end-points and the necessary tilting adjustments were made in order to minimise the location tolerance in the X-direction. The diametric values were obtained from the travel length of the Y-translation stage, with a 1 μm resolution, which was controlled by the personal computer while the laser sensor unit remained stationary.

Typical data for a diametral scan, obtained at the n'th step which is the height (distance) value from the bottom of the green sample, are illustrated in Fig. 4. The measuring step was fixed at 1 μm in the X-direction, the height coordinate. The diameter of the compact was measured from the travel length of the Y-translation stage (see Fig. 3(b)) between the A and D locations (see Fig. 4). The Y-translation stage was moved towards the sample from the location where the sensor indicated an 'out-of-range' signal. The data between the A and B locations were collected at a frequency of 0·1 s while the speed of the Y-translation stage was 10 μms^{-1}. With this procedure a 1 μm resolution for the diameter as a function of height was obtained. In order to obtain rapid measurements, the speed of the Y-translation stage was increased between the locations B and C. The locations B and C were set as target points. The procedure which was used between the A and B locations was repeated for the C and D locations. As a result, the diametric value was calculated from the total travel length of the Y-translation stage between the locations A and D. The measurements were repeated along the axis of the sample.

3 Finite Element Modelling

3.1 Material constitutive model for a ceramic powder

Powder materials exhibit a rather complex response to deformation when subjected to an external loading. A general material constitutive model for a powder material must reflect the major material deformation responses to the action of external stresses. For the present system these major material responses are those of: (i) elastic strain, (ii) permanent volumetric strain, (iii) permanent shear strain, and (iv) strength (yielding, hardening) and failure.

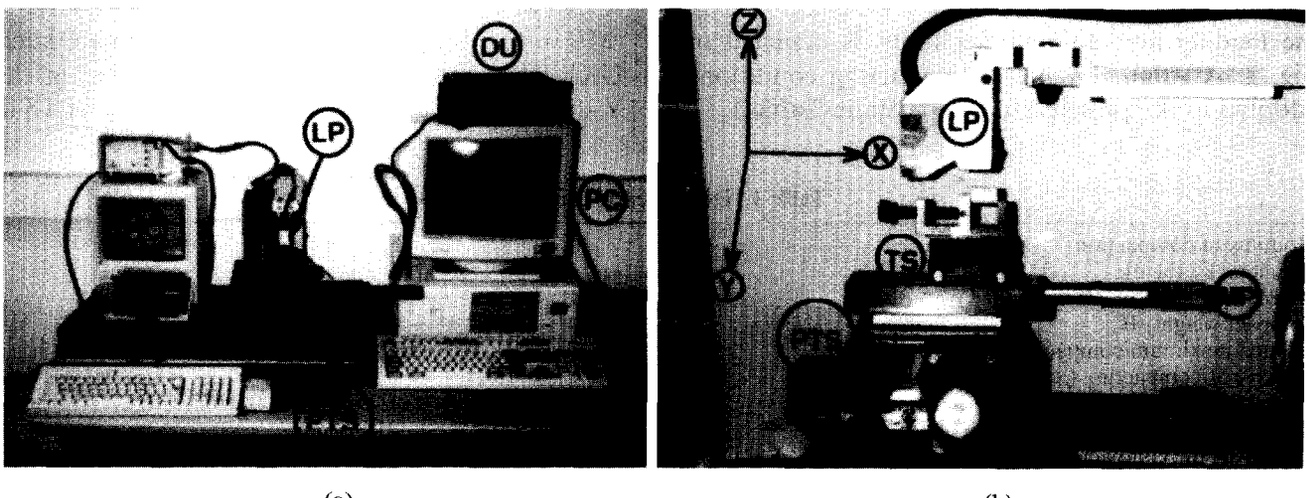

(a) (b)

Fig. 3. Experimental arrangement for the shape measurement by laser profilometry (sample is in the position for diametral scan).

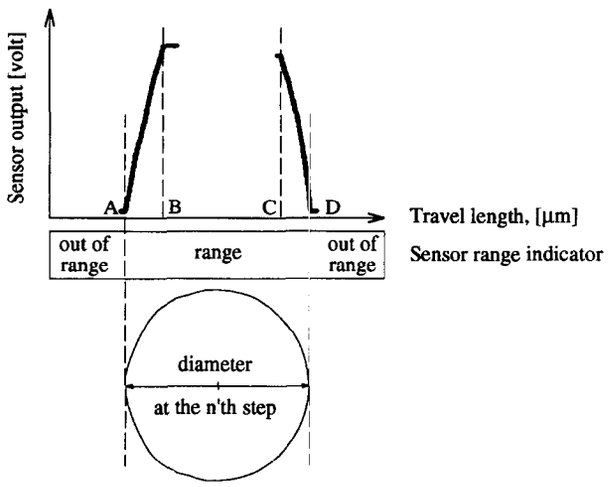

Fig. 4. The diametral scan data; schematic.

Many constitutive models have been developed to describe these responses ranging from phenomenological hydrostatic models to more advanced models based upon plasticity theory. In the current analysis, a generalised 'multi-yield surface function' elasto-plasticity model was adopted to model the uniaxial compaction of the alumina powders. There are various types of 'cap' models available within the class of generalised multi-yield surface function elasto-plasticity models where the yield function is written in different forms. In the analysis to be pursued, the modified Drucker–Prager/cap elasto-plasticity model, provided within the library of the commercially available finite element program ABAQUS,[12] was adopted to describe the internal inhomogeneity and dimensional variability of die-pressed ceramic green components. In this model, the total strain rate, $d\varepsilon$, is first linearly decomposed into the elastic strain rate, $d\varepsilon^{el}$, and the inelastic (plastic) strain rate, $d\varepsilon^{pl}$, components, so that:

$$d\varepsilon = d\varepsilon^{el} + d\varepsilon^{pl} \tag{1}$$

The elastic behaviour is treated as being entirely linear and reversible. For the plastic yield behaviour, the model adopted employs two main segments: a fixed yield surface and a moving yield surface (see below). These two main segments are plotted in a schematic manner in Fig. 5 in a stress space in which the coordinates are the equivalent pressure stress, p, and the square root of the second invariant of deviatoric stress, $\sqrt{J_2'}$, i.e.:

$$p = \frac{1}{3}(\sigma_1 + \sigma_2 + \sigma_3) \tag{2}$$

$$J_2' = \frac{1}{6}[(\sigma_1 - \sigma_2)^2 + (\sigma_2 - \sigma_3)^2 + (\sigma_3 - \sigma_1)^2] \tag{3}$$

where σ_1, σ_2 and σ_3 are the principal stresses (compression assumed positive). There is a transition region between these segments introduced to provide a smooth surface.

The location of the fixed yield surface is taken to be in the form of the Drucker–Prager shear failure surface function,[13,14] $F_{s,D-P}$, providing dominantly shear flow, and is written as:

$$F_{s,D-P} = \sqrt{J_2'} - p\tan\beta - d = 0 \tag{4}$$

where β is the material's internal angle of friction and d is its cohesion (see Fig. 5).

The cap component of the model is used to define the moving yield surface for the proposed model. Initially, the cap model was developed to represent the mechanical behaviour of geological materials.[15,16] DiMaggio and Sandler[15] applied the cap model for computational studies of ground shock and structure–medium interaction effects. Gupta *et al.*[17] applied this model for predicting the failure of concrete under various compressive loadings. However, the model has been extended to study the behaviour of porous and powder materials.[10,18] In the cap model, the cap surface bounds the yield surface in hydrostatic compression, thus providing an essential inelastic hardening mechanism (or response) to represent plastic compaction. The cap action serves to control volume dilatancy when the material yields in shear, by providing a softening, as a function of the inelastic volume increase, created as the material yields on the Drucker–Prager shear failure and transition yield surfaces. The cap yield surface has an elliptical shape with constant eccentricity in the meridional plane (see Fig. 5) and the cap yield surface function, F_c, is written as:

$$F_c = \sqrt{(p - p_a)^2 + \left[\frac{R\sqrt{J_2'}}{(1 + \alpha - \alpha/\cos\beta)}\right]^2} - R(d + p_a\tan\beta) = 0 \tag{5}$$

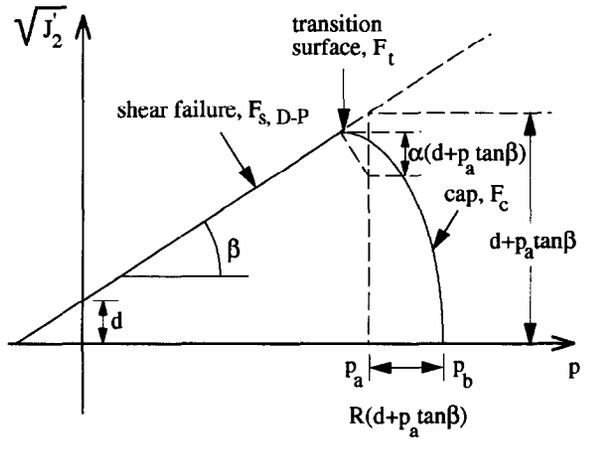

Fig. 5. Drucker–Prager/cap model; yield surfaces in the meridional ($p - \sqrt{J_2'}$) plane.

where R is a material parameter that controls the shape of the cap, α is a small number which is defined below, and p_a is an evolution parameter that represents the volumetric plastic strain driven hardening/softening effects. The hardening/softening law needs to be defined, interrelating the hydrostatic compaction yield stress, p_b, and the corresponding volumetric plastic strain ε_{vol}^{pl} (Fig. 6). The evolution parameter p_a is defined as:

$$p_a = \frac{p_b - Rd}{(1 + R\tan\beta)} \tag{6}$$

The parameter α is a small number (typically 0·01 to 0·05) which is used to define a smooth transition surface between the shear failure surface and the cap. The transition surface function, F_t, is written as:

$$F_t = \sqrt{(p - p_a)^2 + \left[\sqrt{J_2'} - \left(1 - \frac{\alpha}{\cos\beta}\right)(d + p_a\tan\beta)\right]^2} - \alpha(d + p_a\tan\beta) = 0 \tag{7}$$

The overall model assumes associated flow within the cap region and nonassociated flow within the shear failure and transition regions.[12,16]

3.2 Procedure for finite element analysis

The necessary numerical values of the material parameters required for the implementation of the Drucker–Prager/cap model are provided in Table 2. The determination of these parameters has been discussed in detail elsewhere.[9] Mainly, these parameters may be obtained from the information on the stress-strain and principal stresses obtained from the compaction experiment. The yield surfaces (see Fig. 5) and the hardening/softening law (see Fig. 6) are then defined for the implementation of the current model.

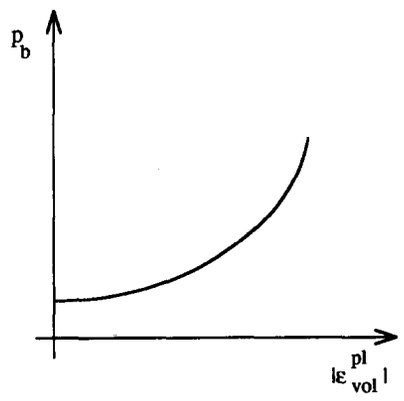

Fig. 6. Typical cap hardening.

Table 2. Drucker–Prager/cap model parameters

Young's modulus, E	9020·0 MPa
Poisson's ratio, v	0·278
Material's cohesion, d	5·5 MPa
Material's internal angle of friction, β	16·5°
Shape factor for the cap, R	0·558
Transition surface factor between the shear failure surface and the cap, α	0·03

Due to the axisymmetric nature of the compaction process, only half of the powder bed was modelled using a set of 8-node (16 degrees of freedom) axisymmetric continuum elements. The initial geometry of the compaction process is shown in Fig. 7(a) together with the boundary conditions. The die wall was modelled as a rigid surface and interface elements were used to define the contact situation between the die wall (rigid surface) and the powder. A conventional Coulombic boundary condition was adopted where a traction coefficient was taken (at the boundary nodes) as the ratio of the wall shear stress to the wall normal stress. Where the wall traction coefficient (shear stress/normal stress) was less than the specified coefficient of friction a stick condition was assumed. If the wall traction coefficient exceeded the chosen friction coefficient the slip condition was invoked. The Coulombic friction coefficient, μ, between the die wall and the powder bed was assumed to be a constant and not a function of the normal stress. In the present paper, the predicted results are given for the chosen friction coefficient value of 0·3.[19,20] The bottom of the material is immovable (fixed) in z-direction during compression. Because of the non-linearity of the problem, an incremental solution was needed in which the upper movement was applied to those nodes at the top as a series of small increments and the corresponding stresses were solved at each step. The total amount of applied movement (displacement), during the compression, is taken as the difference between heights before compaction, Z_0, and that at the maximum applied stress, $Z_{\bar{\sigma}_{max}}$. Initially, the integral stresses were determined using a coarse finite element mesh. Then, the mesh was subsequently refined until further mesh refinement did not change the computed stresses significantly. The final compromise mesh adopted is shown in Fig. 7(b).

Ejection was simulated by sequentially releasing the surface boundary tractions developed during pressing. The implementation of ejection was first applied by removing the upper boundary condition (unloading) after the completion of the pressing. Hence, the compact became free to relax in the z-direction while the compact was still in the die. The removal of the bottom boundary condition and the die wall traction (ejection) was followed as the last

step. Finally, the deformed (relaxed) structure of the green component was obtained.

4 Results and Discussion

4.1 Comparison of experimental and numerical results

The experimental height value for the green compact, $(Z_{EJ})_{exp}$, was obtained from the surface profile scan between the end-points of the cylindrical sample. The predicted height value for the green compact (after ejection), $(Z_{EJ})_{num}$, was calculated from the coordinates of the bottom and top edge nodes. The diametrical values, obtained from the scan data and calculated from the numerical results (from the coordinates of the lateral nodes), were processed by calculating diameter deviation values (diameter–lower limit of diameter) and adding them to the lower limit of the diameter value with a multiplication factor, K. These data were then fed into a mesh generation program (different scales were used in order to conveniently visualise the shape change). Dimensional variations of the cylindrical sample after ejection, measured experimentally and calculated by the finite element modelling, are illustrated in Figs 8(a) and (b), respectively. A comparison of the experimental and numerical shape data, after the ejection, is given in Table 3.

It may be noted from the experimental scan data and the numerically predicted shape of the compact, shown in Figs 8(a) and (b), that there is a significant radial recovery (expansion) upon the lateral surface of the cylindrical alumina sample. The lower limits of the diameter values (LLD) were found to be 12·984 and 12·983 mm, at the bottom of the compact, both from experimental and numerical results, respectively (see Table 1 for the die diameter value). The difference between the lower limits of diameter values, measured experimentally and calculated numerically, is thus *ca.* 1·0 μm; the average expansion of this part of the green is *ca.* 3·5 μm after ejection. Along the surface of the cylindrical axis of the green compact, the diameter values increase up to a certain distance (height) from the bottom of the compact for both the experimental and the numerical results. The upper limit of the diameter (ULD) value was found to be 12·988 mm at a height of between 8 and 10 mm from the bottom of the compact in the experimental scan results (see Fig. 8(a)). For the case of a profile at a height of 10 mm from the bottom, the diametric values decrease towards the top of the green compact where the diametric value was measured as 12·985 mm. From the corresponding numerical simulation results, calculated from the Drucker–Prager/cap finite element analysis, the value of upper limit of the diameter was found to be *ca.* 12·990 mm at a height of 10·4 mm from the bottom of the compact (see Fig. 8(b)). This computed value remained the same till a height of 11·7 mm, from the bottom of the compact, and decreased towards the top at which the numerical diameter value was predicted to be 12·986 mm. The difference in the measured and the predicted height values (here, only the height between the bottom and the top edges is consid-

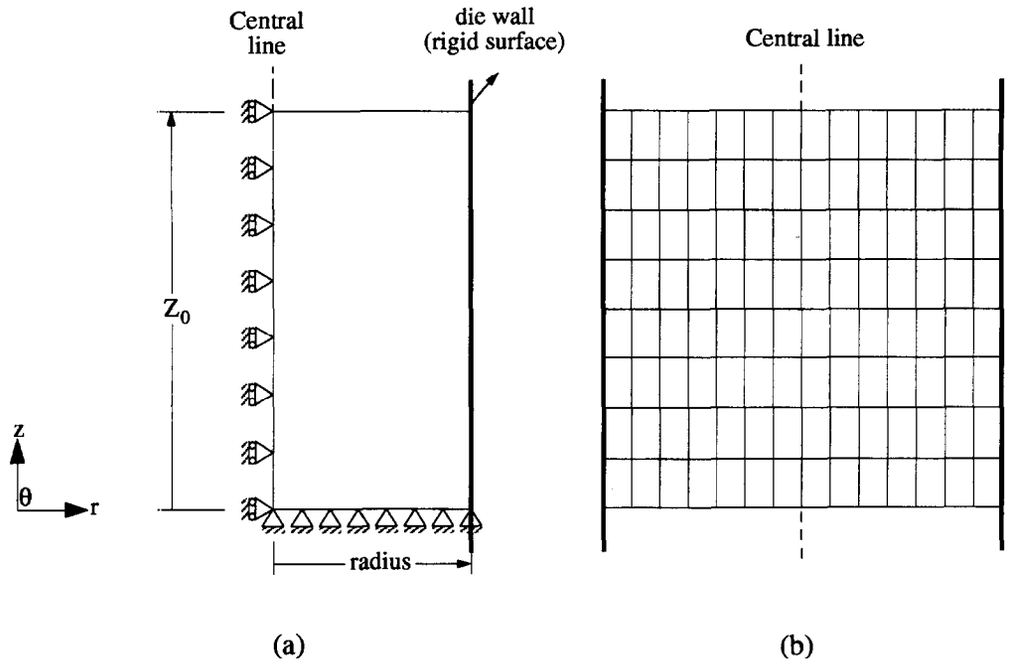

Fig. 7. (a) The geometry of the compaction process with the boundary conditions, (b) final adopted mesh with the axisymmetric angle set to 180°.

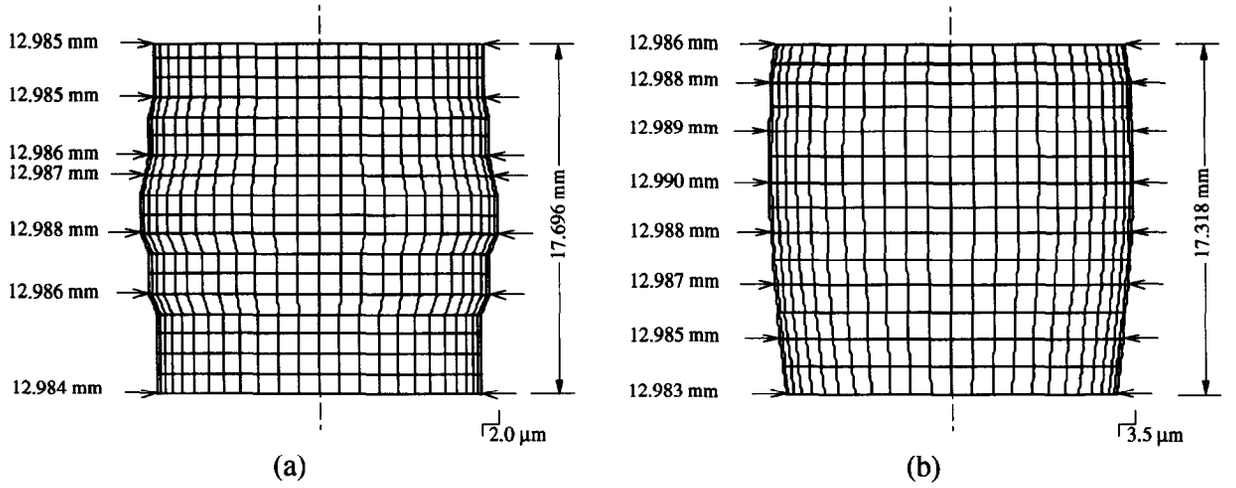

Fig. 8. Dimensional variations of the cylindrical sample after ejection, (a) measured experimentally and (b) calculated numerically ($\mu = 0{\cdot}3$). The measured and predicted height values between bottom and top edges, diametral variation and radial tolerance values are presented. Mesh shows surface nodes only (dimensional variation has a magnification factor of K = 1500 for visualisation purposes).

ered) is 378 μm. The measured and predicted shape results for the green compact are therefore in very good agreement.

4.2 Discussion on the evolution of the dimensional variation of the green compacts during their compaction

The diametric deviation values for the green body were found to be 4·0 and 7·0 μm from the experimental and numerical results, respectively.

The application of the Drucker–Prager/cap finite element analysis enables the construction of a structural inhomogeneity model and the prediction of the dimensional variability of the ceramic compacts to be determined during the entire compaction cycle. Figures 9, 10 and 11 show the predicted equivalent (hydrostatic) pressure, axial and radial stress distributions at maximum applied stress stage, after the removal of top and bottom tractions and the die wall (ejection), during compaction process, respectively. As might be expected, the stress distributions within the green body are not very uniform at the maximum applied stress stage, because of the frictional effects at the die wall boundaries. This internal structural inhomogeneity may be noted in the contour plots of equivalent pressure stress as well as its components in axial and radial directions (see Figs 9(a–c)). Because of the frictional effects at the wall, the level of the transmitted pressure, towards the bottom of the compact, decreases resulting in a decrease of the stress along the axial direction. Larger axial stress variations appear in the upper half than in the lower half of the compact. Specifically, a large stress concentration is seen at the upper corners of the compact.

After the removal of top and bottom punches (top and bottom boundary tractions), the stress distribution within the body changes greatly from the condition imposed at the initial stage (see Fig. 10). It is very clear that, after the removal of upper punch (upper boundary traction), the stored elastic stresses are significantly released in the axial direction. This stress release continues within the compact after the removal of the bottom punch (bottom boundary condition) prior to the ejection causing extension in the axial direction. The most significant result to be noted in the unloading stage was the built-up of the axial tensile stress within the compact associated with the releasing of the top and bottom surface tractions. The variations of the axial tensile stresses at the upper and lower regions of the compact are shown in Fig. 10(b).

Table 3. Experimental and numerical shape data after ejection

Experimental	Height (between bottom and top edges) after ejection, $(Z_{EJ})_{exp}$	17·696 mm
	Upper limit of diameter, $(ULD_{EJ})_{exp}$	12·988 mm
	Lower limit of diameter, $(LLD_{EJ})_{exp}$	12·984 mm
	Diameter deviation, $(DD_{EJ})_{exp}$	4·0 μm
Numerical	Height (between bottom and top edges) after ejection $(Z_{EJ})_{num}$	17·318 mm
	Upper limit of diameter. $(ULD_{EJ})_{num}$	12·990 mm
	Lower limit of diameter. $(LLD_{EJ})_{num}$	12·983 mm
	Diameter deviation. $(DD_{EJ})_{num}$	7·0 μm
Comparison	% difference between $(Z_{EJ})_{exp}$ and $(Z_{EJ})_{num}$	2·100
	% difference between $(ULD_{EJ})_{exp}$ and $(ULD_{EJ})_{num}$	−0·015
	% difference between $(LLD_{EJ})_{exp}$ and $(LLD_{EJ})_{num}$	0·008

Since this accumulated tensile stress is, first, initiated by the removal of the upper punch, the tensile stress may lead to the development of a crack, known as 'capping', at the top surface of the compact. The occurrence of axial tensile stresses within the compact, in the die, as soon as the upper punch is released has also been reported by Rue *et al.*[21] from direct experimentation. While the removal of the punches results in the relaxation in those regions towards the top and bottom faces, the large residual radial stress is at about the middle of the compact (see Fig. 10(c)).

The final green compact takes its form (structural and dimensional) after the ejection (removal of the die wall boundary condition) (see Fig. 11). After the ejection, the compact is freed in the radial direction and the high stress regions relax radially and become higher than those low stress regions near the top and bottom regions. This causes more bulging on the lateral surface (high diameter value) of the compact at the high stress regions about the middle of the compact (see Fig. 8).

At the end of the compaction process, a green body with structural inhomogeneity and dimensional variability is obtained. The residual stresses remain as those shown in Fig. 11 which are markedly different to those at the completion of the compaction shown in Fig. 9.

5 Conclusion

This paper has sought to provide a basis for understanding the formation of the shape of a geometrically simple die-pressed ceramic green compact during a powder agglomerate compaction process. It offers a means of providing quantitative information regarding the die compaction process including the internal structural inhomogeneity and the dimensional variability of these ceramic precursors. This has involved a combination of numerical and experimental studies. The applications of an established elasto-plastic (Drucker–Prager/cap) model to describe dimensional variation of the die-pressed ceramic green compacts combined with the implementation of this constitutive model into finite element code were reported in the numerical part. Sample calculations, based upon the estimated properties of the alumina ceramic powder, illustrate a potential for the improving of the understanding of the die compaction of powdered materials and the final shape formation of the corresponding ceramic green forms. In the experimental part, the preparation of the green body simulated in the numerical study was reported. The dimensional variation of the ceramic green compact, measured by means of non-contacting

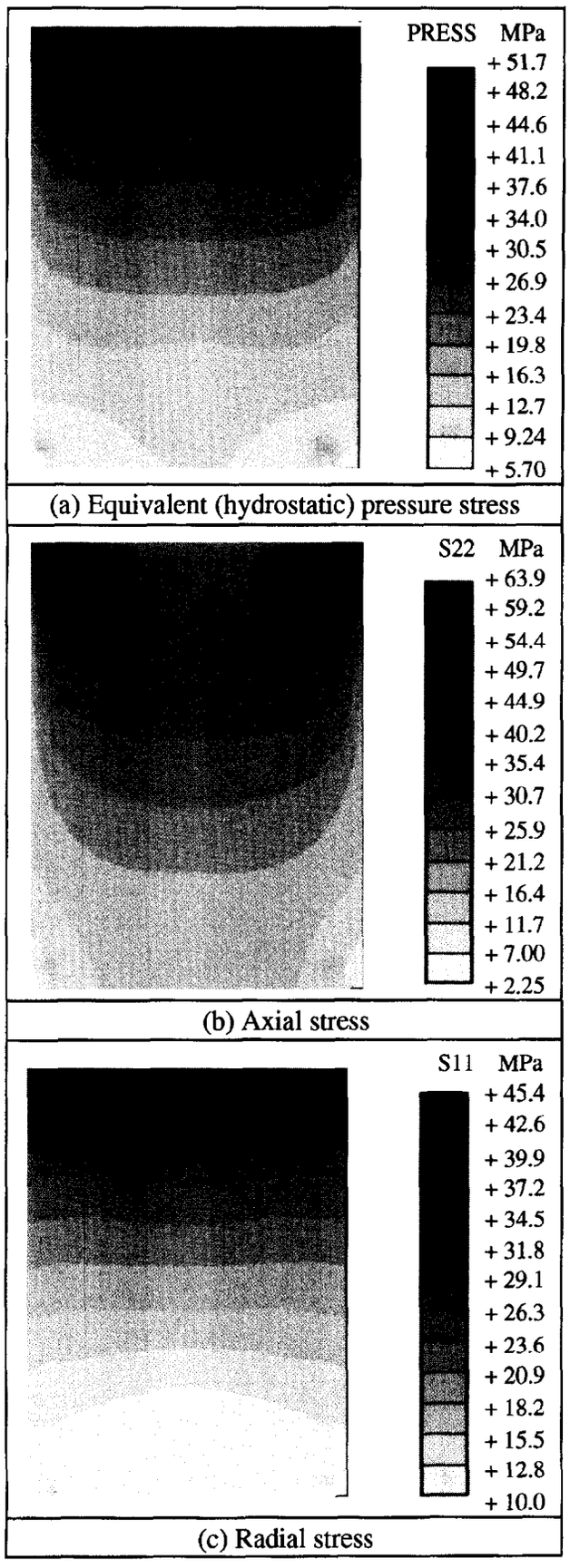

Fig.9. The predicted (a) equivalent (hydrostatic) pressure, (b) axial stress and (c) radial stress distributions, obtained by finite element modelling ($\mu = 0{\cdot}3$), at the maximum applied stress stage during compaction.

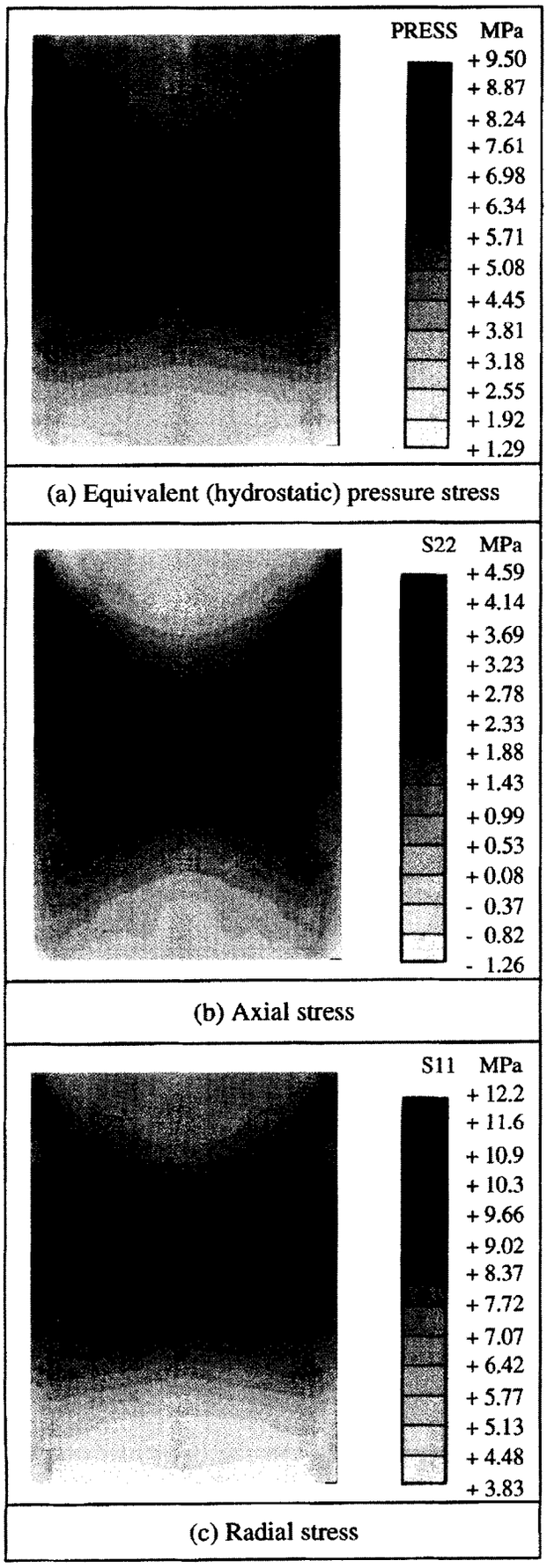

Fig. 10. The predicted (a) equivalent (hydrostatic) pressure, (b) axial stress and (c) radial stress distributions, obtained by finite element modelling ($\mu = 0{\cdot}3$), after the removal of top and bottom boundary tractions during compaction.

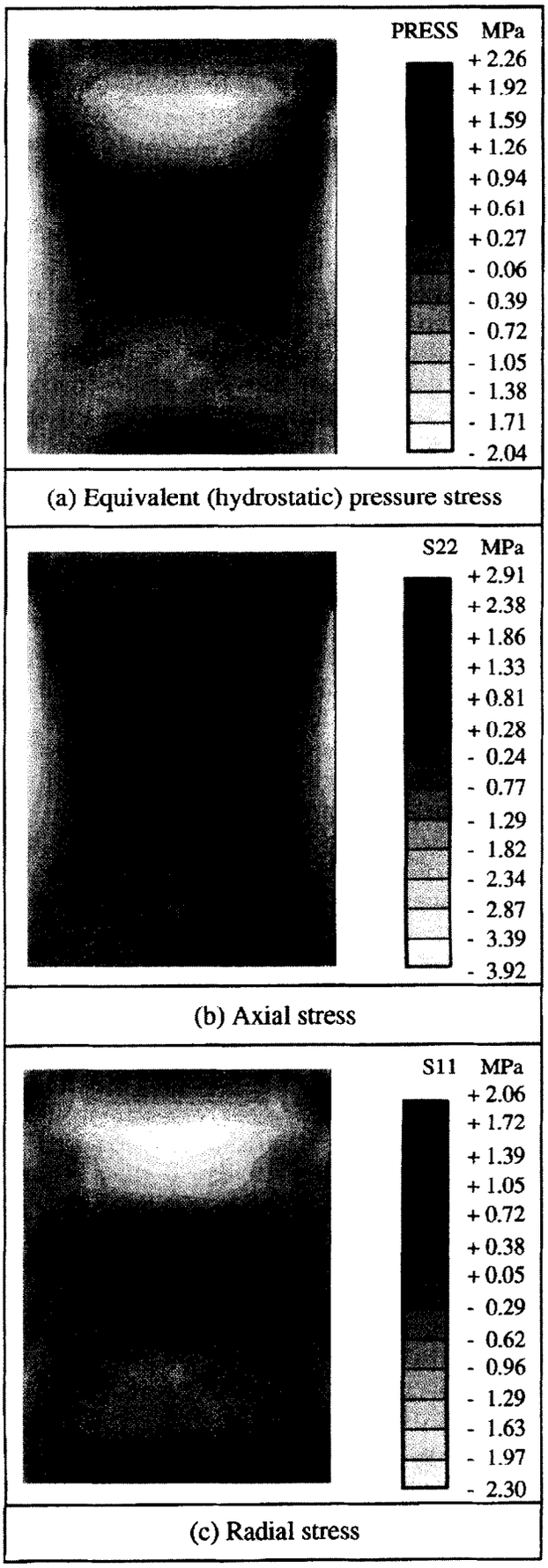

Fig. 11. The predicted (a) equivalent (hydrostatic) pressure, (b) axial stress and (c) radial stress distributions, obtained by finite element modelling ($\mu = 0{\cdot}3$), after the removal of die wall constraint (ejection).

laser profilometry, was described. The predicted shape results, obtained from the numerical model, agree well quantitatively with the corresponding experimental results obtained from investigations of the dimensional variability of the green body. The major conclusion of the paper is that this approach provides a reasonably self-consistent and predictively accurate account of the displacement data of every point (node) within the die-pressed compact from the 'before compaction' to the final 'ejection' stages which may then be used as input data for the mathematical modelling of the mechanism of shape and property changes of ceramic products during densification (sintering) processes in the context of 'near-net-shape forming' of ceramics. A number of subsidiary conclusions may also be drawn:

(1) The geometry of the die-pressed green compact is not exactly the same as, nor indeed is it a simply linear scale transformation of, the die cavity after the ejection.
(2) The diameter of the cylindrical ceramic green compact increases from the bottom of the compact and the upper limit of the diameter exists about the median height of the compact. The diameter value decreases towards the top of the compact. This 'bulging' or 'barrelling' arises from the large residual stresses (mainly the radial component) in the region about the middle of the compact which are created following the removal of top and bottom punches after the compaction process.
(3) Large residual traction stresses remain along the die wall after the complete release of top and bottom surface tractions. The presence of these radial stresses, which promote large wall shear stresses, requires large ejection pressures in order to remove the product from the die. Progressive ejection of compacts out of the die needs to be studied both experimentally and numerically in order to gain detailed insight on the fracture evolution within the green products during ejection.
(4) Tensile zones are predicted in the upper and lower portions of the compact during the removal of top and bottom punches. A crack may thus develop and propagate in the upper region of the compact after the removal of the upper punch prior to the removal of the bottom punch. It may also be inferred that the internal density distributions also change significantly after the initial compaction stage during punch removal and green body ejection.[9]

These subsidiary conclusions apart, the main conclusion is that the finite element calculations of the loading, the unloading and the ejection processes provide the information necessary for calculating the strength, the serviceability and the shape of the compact as well as providing a basis for the optimisation of the overall compaction process, particularly, in the context of near-net-shape forming operations.

References

1. Agarwal, J. C., Process economics and strategies in the advanced ceramics industry. *Adv. Ceram. Mater.*, 1986, **1**, 332–334.
2. Anon, Automatic inspection of nuclear fuel element cans. *Metrology and Inspection*, April/May 1973, 5–8.
3. Shires, G. L. and Dee, C. N., Fluid bearings, with special reference to silicon nitride. *Special Ceramics*, 1972, **5**, 275–282.
4. Broese Van Groenou, A., Compaction of ceramic powders. *Powder Technol.*, 1981, **28**, 221–228.
5. Train, D., Transmission of forces through a powder mass during the process of pelleting. *Trans. Instn. Chem. Engrs*, 1957, **35**, 258–266.
6. Schwartz, E. G. and Weinstein, A. S., Model for compaction of ceramic powders. *Journal of Amer. Ceram. Soc*, 1965, **48**, 346–350.
7. MacLeod, H. M. and Marshall, K., The determination of density distributions in ceramic compacts using autoradiography. *Powder Technol.*, 1077, **16**, 107–122.
8. Broese Van Groenou, A. and Lissenburg, R. C. D., Inhomogeneous density in die compaction: Experiments and finite-element calculations *Comm. Amer. Ceram. Soc.*, September 1983, C-156–C-158.
9. Aydin, I., Briscoe, B. J. and Sanliturk, K. Y., The internal form of compacted ceramic components: A comparison of a finite element modelling with experiment, *Powder Technol.*, 1996, **89**, 239–254.
10. Aydin, I., Near-net-shape forming of ceramics. PhD thesis, University of London, Imperial College of Science, Technology and Medicine, London, UK, 1995.
11. Aydin, I., Briscoe, B. J. and Sanliturk, K. Y., Density distributions during the compaction of alumina powders: A comparison of a computational prediction with experiment. *Comp. Mat. Sci.*, 1994, **3**, 55–67.
12. Hibbitt, Karlsson and Sorensen, Inc., *ABAQUS Theory Manual Version 5.4*, 1994, pp. 4.4.4-1.
13. Drucker, D. C. and Prager, W., Soil mechanics and plastic analysis or limit design. *Quart. Appl. Math.*, 1952, **10**, 157–175.
14. Drucker, D. C., On uniqueness in the theory of plasticity. *Quart. Appl. Math.*, 1956, **4**, 35–42.
15. DiMaggio, F. L. and Sandler, I. S., Material model for granular soils. *Journal of Eng. Mech. Div., ASCE*, 1971, **97**, 935–950.
16. Sandler, I. S., The cap model for static and dynamic problems. In *Site Characterisation*, ed. W. S. Brown, S. J. Green and W. A. Hustrulid. Utah Engineering Experiment Station, Utah, 1976, pp. 1A2-1–1A2-11.
17. Gupta, Y. M., Seaman, L. and Curren, D. R., A generalised plasticity model for predicting failure of concrete. Quarterly progress report 3, Stanford Research Institute, Menlo Park, CA 94625, 1976.
18. Hehenberger, M. and Crawford, J. E., A predictor method for finite element analysis of sliding friction. *Scand. Journal of Metallurgy*, 1983, **12**, 285–288.
19. Brekelmans, W. A. M., Janssen, J. D. and Van de Van, A. A., An Eulerian approach for die compaction process. *Int. J. Numerical Methods in Eng.*, 1991, **31**, 509–524.
20. Frisch, B., Hör, Th., Thiele, W. R., Klemm, U., Sobek, D.

and Stolle, W., Characterisation of ceramic dry pressed bodies—measurement techniques and evaluation. *Ceram. Forum Int.*, 1994, **71**, 24–33.

21. Rue, P. J., Barkworth, P. M. R., Ridgway-Watt, P., Rough, P., Sharland, D. C., Seager, H. and Fisher, H., Analysis of tablet fracture during tabletting by acoustic emission techniques. *Int. Journal of Pharm. Technol. & Prod. Mfr.;1*, 1979, **1**, 2–5.